ELSEVIER

Deep-Sea Research II 52 (2005) 1763–1783

DEEP-SEA RESEARCH
PART II

www.elsevier.com/locate/dsr2

# Determining the applicability of the barotropic approximation to the mean seasonal flow through the Tsushima/Korean Strait using variational assimilation

S.R. Smith[a,*], G.A. Jacobs[a], R.R. Leben[b]

[a]*Naval Research Laboratory, Code 7320, Bldg 1009, Stennis Space Center, MS 39529, USA*
[b]*Colorado Center for Astrodynamic Research, Campus Box 431, University of Colorado, Boulder, CO 80309, USA*

Received 18 August 2002; received in revised form 2 December 2004; accepted 18 December 2004
Available online 21 July 2005

**Abstract**

Variational assimilation is used to combine velocity and sea-surface height anomaly (SSHA) measurements with a system of dynamics to estimate the seasonal flow through the Tsushima/Korean Strait for the summer, autumn, and winter seasons of 1999–2000. The velocity measurements are from two lines of moored acoustic Doppler current profilers (ADCPs) spanning the Tsushima/Korean Strait just north and south of Tsushima Island and the SSHA measurements are from the TOPEX altimeter. The dynamics are the linear, time-independent, shallow-water equations and are forced by winds from the Navy Global Ocean and Atmospheric Prediction System. A weighted least-squares technique is used to determine the seasonal flow fields that simultaneously minimize the weighted residuals of the two data sets and the system of dynamics. The weights are based on expected errors, allowing the assimilation system to put more emphasis on the components of data and dynamics that are known more accurately.

Earlier studies show that the flow through the Tsushima Strait is barotropic throughout most of the year. The region just offshore of the southeast coast of South Korea, however, has been identified as being subject to strong baroclinic processes during autumn. In an attempt to verify this observation, best estimates of the seasonal flow fields are computed by assimilating the two data sets with both a single-layered barotropic system of equations and a 2.5-layered baroclinic system of equations. The minimized residuals of the barotropic system of equations reveal that the solutions satisfy these equations within expected errors throughout most of the domain. Just offshore of the southeast coast of South Korea, however, the barotropic momentum equation residuals exceed 3 times the expected error during autumn, therefore implying that the barotropic approximation is not valid at this location. The 2.5-layered baroclinic momentum equation residuals within this region are smaller than the barotropic residuals, suggesting the existence of baroclinic processes.

Published by Elsevier Ltd.

*Corresponding author. Fax: +1 228 688 4759.
*E-mail address:* smithsc@nrlssc.navy.mil (S.R. Smith).

0967-0645/$ - see front matter Published by Elsevier Ltd.
doi:10.1016/j.dsr2.2004.12.025

## 1. Introduction

The Tsushima/Korea Strait (Fig. 1) is the primary inlet of seawater and advected heat into the Japan/East Sea. The majority of water that flows into the Tsushima Strait originates from the Kuroshio and its properties are distinguished by being relatively warm and saline. Water enters the strait through two different locations. The majority of incoming water enters between Kyushu and Cheju Island and is called the Tsushima Current (TSC). The remaining inflow comes in between Cheju Island and South Korea and is called the Cheju Warm Current (CWC). Tsushima Island divides the incoming water into the eastern and western channels (Fig. 1). The number of distinct

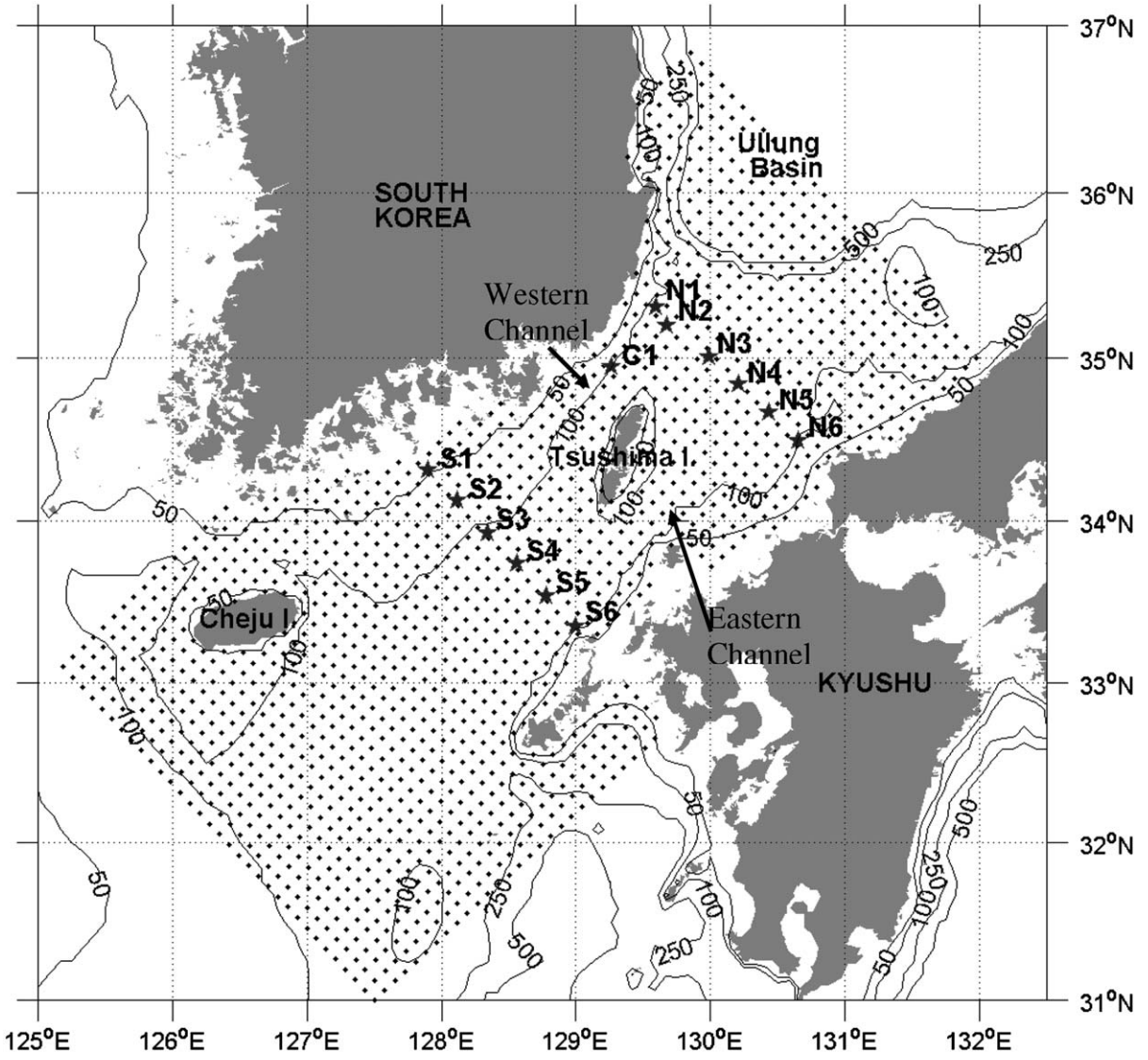


Fig. 1. Map of the Tsushima Strait region where contours indicate bathymetry (m) and the black dots represent the discretized grid at which best estimates of vertically integrated, seasonally averaged velocity and seasonally averaged SSH are computed. Also displayed on this map are the positions of the bottom-mounted ADCPs (gray stars).

currents flowing out of the Tsushima/Korean Strait and into the Japan/East Sea is observed to vary from one to three. The exiting current that is most persistently observed is the Near Shore Branch (NSB). This current is an extension of the TSC, originates from the eastern channel, and flows northward along the coast of Japan (Kim and Legeckis, 1986). The water exiting the western channel typically forms the East Korean Warm Current (EKWC), which flows northward along the Korean continental slope. Observations have been made, however, that show that the EKWC does not exist during winter and spring (Kim and Legeckis, 1986; Cho and Kim, 2000). A third current is occasionally observed at the exit of the Tsushima/Korean Strait and is referred to as the Off Shore Branch (OSB) (Kim and Legeckis, 1986). This current forms as the EKWC begins to turn northward and flow between the coast of Korea and the Ullung Basin. A branching occurs on the downstream side of the strait, and a mass of water flows eastward along the southern edge of the Ullung basin. Continuing alongside the edge of this basin, the mass of water turns northeastward, forms the OSB, and enters into the Japan/East Sea flowing parallel to the NSB.

The origin, branching, and properties of the flow through the strait have been observed to have substantial seasonal and interannual variations. The average transport through the strait is roughly 3.5 Sv ($1\,\mathrm{Sv} = 10^6\,\mathrm{m}^3/\mathrm{s}$) (Miita and Ogawa, 1984). This transport, however, has been observed to vary from 5.6 Sv in September to 1.2 Sv at other times (Isobe et al., 1994). In addition, since this strait is only about 250 km across with depths typically less than 150 m, the flow through the strait is subject to a strong constraining influence by the coastlines. The Rossby Radius of deformation is approximately 18 km (Cho and Kim, 1998). Strong seasonal variations in surface forcing, such as wind stress and heat flux, also play an important role in causing the environment within the strait to change. Since the bathymetry within the strait is shallow, surface forcing is able to penetrate and influence a majority of the water column. During winter, when the wind stress is at its maximum and the transport is at its minimum, the water within the strait is well-mixed and the flow is observed to be barotropic. Whereas, during summer and autumn, when surface forcing is relatively weak and the transport swift, a strong thermocline at 30–40 m depth is observed (Jacobs et al., 2001b). Isobe (1995) and Cho and Kim (1998) hypothesize that baroclinic processes are prevalent during these warmer seasons, especially at the exit of the western channel.

In an attempt to verify these baroclinic processes and to estimate the seasonal flow through the strait, an approach is used to obtain a solution that best fits prescribed dynamics and measurements in a weighted least squares sense (variational assimilation). Two sets of measurements contribute to the assimilation. The first set includes velocity measurements from an array of moored acoustic Doppler current profilers (ADCPs) deployed during summer, autumn, and winter of 1999–2000. The second set is seasonal sea-surface height (SSH) change inferred from TOPEX altimeter data. A description of these two sources of data, including the processing and preparation for assimilation, is given in the next section. The dynamics that the solution is constrained to follow is described in Section 3. Two sets of numerical dynamics are used to test the accuracy of the barotropic approximation in the strait. These dynamics are the linear, time-independent, shallow-water equations and boundary and smoothing constraints for both a single-layered barotropic system and a 2.5-layered baroclinic system.

A solution is constructed that simultaneously minimizes the dynamic and data residuals, where the residuals are the misfits of the numerical representation of the dynamic and data caused by a particular solution. These residuals are combined into a cost function, such that, given an estimate of the flow field, the cost function provides a single scalar value that represents the total misfit to dynamics and data. The optimal solution is determined by performing a direct variational minimization of this cost function, which amounts to solving a weighted least squares problem (Le Dimet and Talagrand, 1986). In order to properly construct a solution, the weighting of the data and dynamical equations must be correctly specified in the cost function. This is done by estimating the level of weight (inverse of

the expected error covariance) for each component. Certain methods are available to determine expected error covariances. The expected errors of the measurements can be determined directly, whereas the error levels of the dynamical equations are more difficult to quantify. Therefore, it is necessary to test a range of expected error levels to ensure that the solution is not overly sensitive to the specified weights. This assimilation method, including the specification of the expected errors, is described in Section 4.

The seasonal circulation fields resulting from the assimilation of both ADCP and TOPEX data with the barotropic system of equations are presented and discussed in Section 5. To demonstrate the impact that these two data types have on the solution and its cost function, results from assimilating three different configurations of just ADCP data are also presented and discussed. Since these solutions are least-squares fits to observations and dynamics, they satisfy neither exactly. Examination of the dynamic residuals reveals where and during which seasons the solution deviates significantly from the prescribed equations of motion. These results suggest that the flow through the Tsushima/Korean Strait is mostly barotropic. The barotropic momentum equation residuals, however, are significantly high during autumn near the exit of the western channel. Since these residuals far exceed expected values, it is implied that baroclinic processes might be an important contributor in this region. Support for this hypothesis is provided by comparing these residuals with the residuals resulting from using a system of 2.5-layered baroclinic equations. Analysis of this comparison reveals that the solutions satisfy the baroclinic momentum equations better than the barotropic momentum equations, especially in the region and during the season where baroclinic processes are suspected.

## 2. Assimilated data

In this study, two types of data are used in the estimation of seasonal circulation fields (Fig. 2). The first data set is comprised of seasonally averaged vertically integrated velocities derived from moored current meter data (vertically integrated velocity is hereinafter referred as transport). The second set of data is seasonal SSH differences inferred from TOPEX range measurements. Even though these two data sets represent different features and have different levels of accuracy, by using variational assimilation the relative accuracy is accounted for in the weighting used in the least-squares process (discussed in Section 4.3).

### 2.1. Velocity measurements from ADCP moorings

The velocity measurements are obtained from 13 bottom mounted ADCP moorings deployed by the Naval Research Laboratory. Due to the high concentration of fishing and trawling that occurs throughout the strait, it has been difficult in the past to deploy moorings over long periods of time. In order to overcome this problem, trawl resistant bottom mounts (called Barnys after their barnacle-like shape) were used. The exposed side of these dome-shaped mounts is relatively smooth in order to minimize snagging by fishing nets and lines, and the instrumentation is enclosed safely within the dome. Each mooring was equipped with a RD Instruments Workhorse ADCP operating at 300 KHz (Perkins et al., 2000). These moorings were deployed in May of 1999 and spanned the width of the Tsushima Strait just northeast and southwest of Tsushima Island (Fig. 1). An additional mooring was deployed in October of 1999 in the western channel (mooring C1).

The moorings were recovered in March of 2000, and all data was available and used except from moorings N1 and C1 during summer and autumn, and mooring S5 during winter. The collected data consists of both $u$ (eastward) and $v$ (northward) components of velocity with individual samples containing an RMS error of 1 cm/s. The temporal resolution of these samples is 15 min at stations S5, N2, and N3, and 30 min at the other stations. The vertical resolution is 2 m at stations S1, S2, and N2, and 4 m at the other stations. With bottom-mounted ADCPs, however, measurements close to the surface are not useable due to contamination of the acoustic signal by surface interference. The

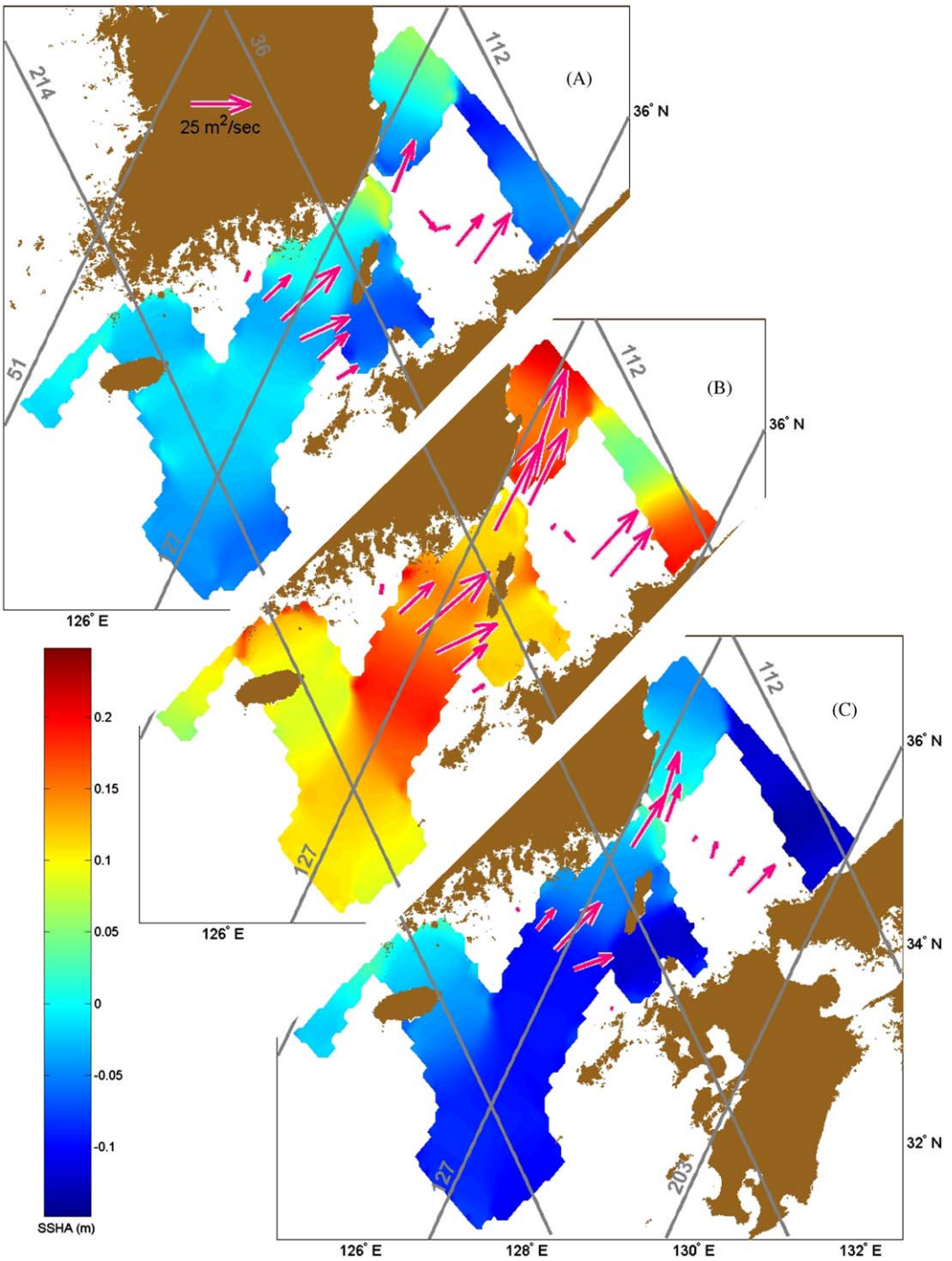


Fig. 2. Sea-surface height anomaly (SSHA) measurements from the TOPEX altimeter (colored contours) and vertically integrated velocity measurements from the bottom mounted ADCPs (red vectors) are seasonally averaged for (A) summer, (B) autumn, and (C) winter of 1999–2000. The SSHA is an interpolation of TOPEX measurements to all discretized grid points (Fig. 1) within 50 km of TOPEX groundtracks (numbered gray lines). The interpolation used is a linearly weighted average based on distance to the data points.

distance from the surface at which this interference occurs varies with instrument deployment depth. The relatively deep ADCPs (about 140 m) were able to measure currents to within 20 m of the surface, whereas the ADCPs in the shallower regions (about 100 m) were able to measure currents to within 10 m of the surface (Jacobs et al., 2001a).

Tidal variability within the strait accounts for 20–60% of the velocity variability depending on the depth and mooring location (Teague et al., 2001). Since this study is concerned with just the nontidal variability, tidal currents and currents near the tidal semidiurnal and diurnal frequencies are removed from the ADCP data using a low-pass filter with a 40-h cutoff frequency (Teague et al., 2002). The measurements of $u$ and $v$ at each location are vertically integrated over either the entire water column for the barotropic system or each of two layers for the baroclinic system. These transports are then rotated 43° in the counterclockwise direction so that the $u$ component is in the along-strait direction to match the discretized grid (Fig. 1). Finally, these measurements are seasonally averaged over summer, autumn, and winter of 1999–2000 (Fig. 2). The seasonal periods are chosen by examining the total transport through the strait. Distinct transitions in the transport are observed between seasons. The transition between summer and autumn occurs rapidly, whereas the transition between the autumn and winter transport is relatively slower and requires about a month to occur (Teague et al., 2002). The dates that are best separated by these transitions are: summer (5/15/1999–8/15/1999), autumn (8/15/1999–11/15/1999) and winter (12/15/1999–3/15/2000).

### 2.2. Sea surface height measurements from the TOPEX altimeter

Seasonal differences in SSH are inferred from processed TOPEX data that are in terms of sea-surface height anomaly (SSHA). Since the TOPEX orbit and range measurements are known accurately, 3.5 and 3.2 cm, respectively, the sea level relative to the Earth reference ellipsoid can be determined with an accuracy of 4.7 cm (Fu et al., 1994). Unfortunately, this measured sea level gives little useful information in regards to the SSH associated with dynamic motion. In order to obtain this information, the geoid height must be subtracted from the sea level. The geoid height is the distance from the reference ellipsoid to the geopotential surface (the ocean surface if it were at rest with no forcing). However, since this geoid height is not known accurately, a time-average of all sea-level measurements made from the first 8 years of the TOPEX/Poseidon mission is used instead. This mean sea level contains both the geoid and the mean height due to ocean circulation. Therefore, deviations from this mean are SSH anomalies (SSHA). These processed TOPEX data are a product of the Naval Research Laboratory and are described in Jacobs et al. (2002).

There are six TOPEX groundtracks within the vicinity of the Tsushima/Korean Strait (Fig. 2). The TOPEX data that are used include all available SSHA measurements during the same time period that the moorings were deployed (cycles 245–276, where each cycle encompasses approximately 10 days). For each cycle, a weighted average of all SSHA measurements at groundtrack points within 50 km of each model grid point is used to compute the SSHA on the model grid. The weight decreases linearly from one at 0 km from the groundtrack point to zero at 50 km distance. The gridded SSHA data, which includes 976 grid points, is seasonally averaged over the same time periods that are used with the velocity measurements (Fig. 2). Directly assimilating this gridded SSHA data, however, can result potentially in significant error. To avoid this error, seasonal differences in SSHA are computed between autumn and summer, and autumn and winter, and used in the assimilation. By using seasonal SSHA differences, the reference level needed to infer SSH becomes irrelevant. There are two drawbacks to this approach; the first is that all three seasonal solutions must be solved simultaneously, thus increasing the computational burden. The second drawback is that there are no direct SSH measurements within the assimilation, therefore allowing the SSH solutions to be biased by a value that is constant in space time.

Table 1
Description of the variables and constants found in the barotropic shallow water equations (Eqs. (1)–(3))

| Element | Name | Units | Value |
|---|---|---|---|
| $U$ | Vertically integrated, seasonally averaged velocity in the along-strait direction | $m^2/s$ | Solution variable |
| $V$ | Vertically integrated, seasonally averaged velocity in the across-strait direction | $m^2/s$ | Solution variable |
| $\bar{\eta}$ | Seasonally averaged sea surface height | m | Solution variable |
| $f$ | Coriolis parameter | 1/s | Prescribed function |
| $g$ | Gravity | $m/s^2$ | 9.81 |
| $H$ | Depth | m | Prescribed function |
| $K_H$ | Horizontal eddy viscosity coefficient | $m^2/s$ | 1000 |
| $\tau_x$ | Wind stress in the along-strait direction | $N/m^2$ | Prescribed function |
| $\tau_y$ | Wind stress in the across-strait direction | $N/m^2$ | Prescribed function |
| $\rho_0$ | Average density | $kg/m^3$ | 1024.24 |
| $C_D$ | Bottom drag coefficient | | 0.002 |
| $\lvert\vec{\bar{u}}_B\rvert$ | Average magnitude of bottom velocity | m/s | Prescribed function |

## 3. Dynamics

### 3.1. Single-layered barotropic equations of motion

The equations of motion used to describe the flow within the single-layered barotropic system are based on the shallow-water equations. The governing physics in this system are the conservation of mass and momentum. These equations are a simplification of the fundamental Eulerian equations of motion that emphasize motions with large horizontal length scales compared to the vertical scale ($L_X, L_Y \gg L_Z$). In addition to the hydrostatic assumption, Boussinesq and linear approximations are also applied. These simplified equations of motion are Reynolds averaged over seasonal time scales so that the time rate of change of all variables is neglected and the equations represent the dynamics of the seasonally averaged flow fields,

$$\frac{\partial U}{\partial x}+\frac{\partial V}{\partial y}=0, \tag{1}$$

$$fV-gH\frac{\partial\bar{\eta}}{\partial x}+K_H\left(2\frac{\partial^2 U}{\partial x^2}+\frac{\partial^2 U}{\partial y^2}+\frac{\partial^2 V}{\partial x\partial y}\right)-\frac{C_D|\vec{\bar{u}}_B|U}{H}=-\frac{\tau_x}{\rho_0}, \tag{2}$$

$$-fU-gH\frac{\partial\bar{\eta}}{\partial y}+K_H\left(\frac{\partial^2 V}{\partial x^2}+2\frac{\partial^2 V}{\partial y^2}+\frac{\partial^2 U}{\partial x\partial y}\right)-\frac{C_D|\vec{\bar{u}}_B|V}{H}=-\frac{\tau_y}{\rho_0}, \tag{3}$$

where $U$, $V$ and $\bar{\eta}$ are the transport components and SSH, respectively.

Each of the variables and constants in Eqs. (1)–(3) is listed along with their units and values in Table 1. The Coriolis parameter ($f$) is considered a function of latitude. The horizontal eddy-viscosity coefficient ($K_H$) is highly dependent on the problem and can have a wide range of values. Therefore, the value of $K_H$ is estimated by considering the values and grid resolution used in many existing models. The average density ($\rho_0$) is estimated using the Modular Ocean Data Assimilation System (MODAS), which is described in Section 3.2. The value chosen for the bottom drag coefficient ($C_D$) is a commonly used value for the sea floor (Csanady, 1984). The average magnitude of bottom velocity ($|\vec{\bar{u}}_B|$) is estimated for each season individually by averaging all ADCP velocity measurements within the bottom 10 m of the water column. The bathymetry ($H$), which is a product of the Naval Research Laboratory, has a 1/12° resolution and is interpolated to the grid using a bicubic spline fit. The wind stresses ($\tau_x$ and $\tau_y$) come from the Navy Global Ocean and Atmospheric

Prediction System which has a spatial resolution of 1° and a temporal resolutions of 6 h. This data set is interpolated to the model grid points using a bicubic spline and seasonally averaged over the same dates as the measurements.

### 3.2. 2.5-Layered baroclinic equations of motion

The baroclinic system of equations differs from the barotropic system in that density is no longer considered constant, therefore allowing the density to provide internal pressure gradients. For example, by allowing the density to be a function of $x$, $y$, layer, and season, the pressure gradient term in Eq. (2), becomes

$$gH\frac{\partial\bar{\eta}}{\partial x} \rightarrow gh_1\left(\frac{\bar{\eta}_1-\bar{\eta}_2}{2\rho_1}\frac{\partial\rho_1}{\partial x}+\frac{\partial\bar{\eta}_1}{\partial x}\right)-\frac{gh_1^2}{2\rho_1}\frac{\partial\rho_1}{\partial x} \quad (4)$$

for the first layer of the baroclinic system, where $h_1$ is the reference thickness of layer 1, $\bar{\eta}_1$ is the SSH, and $\bar{\eta}_2$ is the deviation of the interface between layers 1 and 2.

The baroclinic system of equations is split into three layers with the bottom layer being at rest ($U_3 = V_3 = 0$). The only influence that the bottom layer has on the equations of motion is that the deviation of the interface between it and layer 2 ($\bar{\eta}_3$) affects the thickness and the limits of vertical integration of the second layer. Therefore, the equations of motion are only applied to the first two layers, resulting in seven unknown variables ($U_1$, $V_1$, $\bar{\eta}_1$, $U_2$, $V_2$, $\bar{\eta}_2$, and $\bar{\eta}_3$) that need to be solved for at each grid point. The reference thickness of layer 1 ($h_1$) is chosen such that it approximately contains the mixed layer that is apparent during summer and autumn. Through examination of the MODAS data, the average depth of this mixed layer is roughly $h_1 = 45$ m. The reference thickness of layer 2 ($h_2 = 130$ m) is chosen such that the only places where the bottom layer exists within the gridded domain are the deep basin that is west of Kyushu and the Ullung basin (Fig. 1).

The densities and density gradients in the baroclinic momentum equations are computed independently of the inverse problem using MODAS. MODAS is one of the present US Navy standard tools for production of static, bimonthly, three-dimensional grids of temperature and salinity using all available historical observations. Further details regarding this system are provided in Fox et al. (2002). The grid resolution of the data set produced by this tool for the Tsushima Strait region is 1/8° along the horizontal plane and every 10 m up to 50 m depth and then every 50 m deeper than 50 m. Densities are computed from this climatological data set using the international equation of state of seawater, 1980 (Pond and Pickard, 1983). The density data at each depth interval are interpolated to the grid points using a bicubic spline fit. Finally, by seasonally and vertically averaging the interpolated data set for each layer and season, the functions $\rho_1$ and $\rho_2$ are computed. The horizontal gradients of $\rho_1$ and $\rho_2$ are computed using first-order accurate finite differencing.

### 3.3. Physical constraints

In addition to continuity and momentum, two additional constraints are included in both systems of dynamics. The first constraint forces the cross-shore component of flow to be zero at the solution grid points that border land. This constraint is enforced through satisfaction of the following equation:

$$U\hat{n}_x + V\hat{n}_y = 0, \quad (5)$$

where $\hat{n}_x$ and $\hat{n}_y$ are the normal components in the along and cross-strait directions, respectively, of the vector perpendicular to the coastline. These normal vector components are calculated using the normalized gradients of bathymetry.

$$\hat{n}_x = \frac{\partial H/\partial x}{\sqrt{(\partial H/\partial x)^2+(\partial H/\partial y)^2}},$$
$$\hat{n}_y = \frac{\partial H/\partial y}{\sqrt{(\partial H/\partial x)^2+(\partial H/\partial y)^2}}, \quad (6)$$

For the case of the 2.5-layered system, this boundary constraint is applied to both layers. All of the domain boundary grid points that border water are considered open and have no constraint.

The second constraint is smoothing and its purpose is to remove features that can not be resolved by the discretized grid or the measurements. In order to prevent these unresolved small features in the solution, smoothing is imposed by constraining the Laplacian plus a second-order cross derivative of each of the solution variables to equal zero.

$$\frac{\partial^2 U}{\partial x^2}+\frac{\partial^2 U}{\partial y^2}+\frac{\partial^2 U}{\partial x \partial y}=0, \tag{7}$$

$$\frac{\partial^2 V}{\partial x^2}+\frac{\partial^2 V}{\partial y^2}+\frac{\partial^2 V}{\partial x \partial y}=0, \tag{8}$$

$$\frac{\partial^2 \bar{\eta}}{\partial x^2}+\frac{\partial^2 \bar{\eta}}{\partial y^2}+\frac{\partial^2 \bar{\eta}}{\partial x \partial y}=0. \tag{9}$$

Without this constraint, the solution could be filled with many sub-observation-scale features not resolved by the measurement arrays. For example, given a fine numerical grid with a coarse set of measurements, a small feature that satisfies the dynamics can be placed between the measurement positions without affecting the solution at the measurement locations. The distance between the ADCP moorings is roughly 25 km, and previously observed currents have scales of 28–37 km (Katoh, 1993). Therefore, the ADCP measurements can be expected to resolve the dominant features within the vicinity of the moorings. For the case of the 2.5-layered system, the smoothing constraints in Eqs. (7) and (8) are applied to the upper two layers, and Eq. (9) is applied to all three layers.

## 4. Method

### 4.1. Domain

Solutions to the seasonally averaged transports and SSH are computed on a discretized grid (Fig. 1). Since the Tsushima/Korean Strait is not aligned in either the meridional or zonal direction, the domain is rotated 43° in the counterclockwise direction so that the local $x$-axis of the domain is in the along-strait direction. This is done to minimize the number of grid points required to represent the region adequately while maintaining relative ease in the computer implementation of the numerical solution. The domain consists of 62 grid points in the along-strait direction, and 33 in the cross-strait direction with a grid spacing of $\Delta x = \Delta y = 10$ km. The resulting arrangement of grid points is somewhat irregular due to landmasses and islands. Grid points are removed from the surface layer if they are on land or in water with depths less than 10 m. As for the second and third layer, grid points are removed if the depth is less than the thickness of the layer above it. Also, grid points that are not a part of at least four contiguous water grid points in both the along and cross-strait directions are neglected (four consecutive grid points are required in order to perform a second-order accurate finite difference operation at a boundary point). Application of this masking to the domain results in 1545, 1450, and 179 grid point locations in the surface, middle, and bottom layers, respectively, at which solutions are sought for each of the three seasons. Therefore, the total number of unknowns that need to be solved for in the barotropic and baroclinic systems are 13,905 and 27,492, respectively.

### 4.2. Weighted least squares

The solution is defined as the set of seasonally averaged transports and SSH that minimizes the cost function, which contains the weighted residuals of the discretized equations of motion, physical constraints, and measurements. The equations of motion (Eqs. (1)–(3)) and smoothing constraints (Eqs. (7)–(9)) are discretized at each grid point for each of the three seasons. The derivative terms in these equations are discretized using second-order accurate finite differencing. The boundary constraint (Eq. (5)) is used only at the grid points that border land. Contributions to the cost function due to residuals between the ADCP measurements and solution are applied at the grid points closest to each of the ADCP mooring locations; whereas, the SSHA difference measurements are applied at the locations of the interpolated SSHA (Fig. 2). Since the SSHA difference data involve more than one season, the equations for all three seasons must be solved

simultaneously, therefore resulting in roughly 30,000 equations for the barotropic system.

The barotropic system of independent equations (30,000) provides a number of equations greater than the number of unknowns (13,905). The solution to this problem is determined using the weighted least squares. To begin, the system of linear discretized equations can be written in matrix form

$$\mathbf{Ax} = \mathbf{b}, \tag{10}$$

where **A** is the coefficient matrix which contains the discretization of the left-hand side of the momentum, continuity, boundary, smoothing, and measurement equations. The state vector (**x**) contains the 13,905 unknown variables for which a solution is sought ($U$, $V$, and $\bar{\eta}$ at all grid points), and the forcing vector (**b**) consists of the right-hand side of all the equations. For example, the $x$-momentum equation (Eq. (2)) applied at a particular grid point is contained in one row of **A**, and the wind stress at this grid point specifies one element of **b**.

All of these discretized equations, however, have at least some error associated with them.

$$\mathbf{Ax} - \mathbf{b} = \mathbf{e} \tag{11}$$

The task at hand is to determine the solution (**x**) that minimizes the residuals (**e**). To accomplish this, the residuals are combined into a total cost function in a weighted least-squares fashion,

$$\text{Cost Function} = J(\mathbf{x}) = (\mathbf{Ax} - \mathbf{b})^{\mathrm{T}}\mathbf{W}(\mathbf{Ax} - \mathbf{b}), \tag{12}$$

where **W** is a weighting matrix that places emphasis on the equations that have smaller expected errors. The minimum of this cost function is determined by setting the first variation with respect to the state equal to zero.

$$J(\mathbf{x} + \delta\mathbf{x}) - J(\mathbf{x}) = 0. \tag{13}$$

By taking the limit of this equation as $\delta\mathbf{x} \to 0$, the weighted least-squares formulation is produced.

$$\mathbf{A}^{\mathrm{T}}\mathbf{WAx} = \mathbf{A}^{\mathrm{T}}\mathbf{Wb}. \tag{14}$$

For this study, an iterative conjugate gradient technique is used to solve Eq. (14). This conjugate gradient method is a relaxation method that begins with an initial state of all zeros and seeks out the final state by moving in search directions that are constructed by the conjugation of the residuals ($\mathbf{Ax} - \mathbf{b}$). The conjugate gradient method is beneficial since the search directions do not have to be stored in memory; once a new search direction is computed, the old one is forgotten. In addition, the conjugate gradient method is able to take advantage of the sparseness of the normal matrix ($\mathbf{A}^{\mathrm{T}}\mathbf{WA}$) in Eq. (14). The normal matrix, however, is ill-conditioned since the ratio between the largest and smallest eigenvalue is very large, and at least one eigenmode is known to be ill-posed. This ill-posed eigenmode is present due to the lack of direct SSH measurements, thus causing the overall magnitude of the SSH solution to be dependent on the initial state. Even though this inverse problem is ill-conditioned and contains an ill-posed eigenmode, best estimates of the flow field can be computed and provide reliable information (Wunsch, 1996; Thacker, 1992).

To test the consistency of the solution, dozens of experiments are performed. In each of these experiments, a different initial state is constructed using a random number generator and then used to initialize the conjugate gradient. As expected, the magnitude of the SSH solution varied substantially from experiment to experiment. However, the spatial and temporal gradients of the SSH solution and the transport solution never varied by more than 15% of the original solution. The accuracy of the final solution is dependent on the number of iterations through the conjugate gradient. Theoretically, for a problem that is well-conditioned, this routine should be able to converge to a solution in a number of iterations that is equivalent to one to three times the length of the state. However, since the problem posed in this study is ill-conditioned, which means there are many solutions that are close to the best solution, the conjugate gradient requires many times this number of iterations to navigate to the absolute minimum cost within the machine's precision error. This is discussed further in Section 5.2.

### 4.3. Weighting matrix

One of the most important aspects of any inversion or statistical estimation scheme is the covariance errors or the weight used in the cost function. Once the idealized physical processes are embedded within the dynamical equations, additional constraints applied, and measurements taken, some thought and care must be placed into deriving the appropriate expected error ($\langle er \rangle$). These errors should take into account the neglected terms in the dynamic equations, errors in forcing, errors in the measurements, and representativeness errors (Daley, 1993). After the solution is obtained, the residuals in the dynamical equations are compared to the estimated expected errors to determine if the solution is in agreement with the initial error estimates. If the residuals of the dynamics are greater than the a priori error estimates, then there must be additional contributors to the residuals that were not originally considered.

The weighting matrix that is used in this assimilation is a diagonal matrix whose elements consist of the reciprocal of the expected variance $1/\langle \mathrm{er}^2 \rangle$ for each corresponding dynamical equation. This means that the cross-covariance of the expected errors are neglected. For simplicity, it is also assumed that the expected variance for each of the equations of motion, constraints, and measurements are the same at all grid points and during all seasons.

In order to maintain the correct proportion of weights within the total cost function so that they are independent of the number of grid points or measurements, the weight for each dynamical equation is divided by its number of discretized equations for each season. For example, the continuity weight is defined as

$$W_{\mathrm{Continuity}} = 1/(n_{\mathrm{Continuity}} \langle er^2 \rangle_{\mathrm{Continuity}}), \qquad (15)$$

where $n_{\mathrm{Continuity}}$ is the number of points at which the continuity equation is applied. $n$ is also equal to the number of grid points for the momentum equations and smoothing constraints. For coastal boundary constraints and measurements, $n$ is the number of grid points that border land and the number of measurements that are assimilated for each season, respectively. This definition of the weights assures that each contribution to the cost function can be modeled as a chi-squared variable with an expected value of one and is of comparable magnitude. For example, if the contributions to the cost function are not divided by $n$, a doubling of resolution would place greater weight by a factor of four on the dynamical equations.

Optimally, the expected error associated with each of these dynamical equations should include all of the error resulting from neglected terms, approximations, and discretization. Since it is nearly impossible to account for all of the sources of error within each dynamical equation, the estimation of the expected errors entails some error. Therefore, the expected error associated with each set of dynamical equations is approximated by only considering the primary source of error.

The primary source of error in the continuity equation (Eq. (1)) is a result of neglecting the time rate of change of SSH ($\partial\bar{\eta}/\partial t$). This term is estimated by seasonally averaging the TOPEX data at each of the data points within the region. Then, at each data point the SSHA differences between consecutive seasons are computed. Averaging the magnitudes of these differences results in a mean seasonal SSHA difference of $\Delta\bar{\eta} = 17.67\,\mathrm{cm}$. The estimated value for the neglected term $\partial\bar{\eta}/\partial t$, and hence the estimated expected error of continuity is given in Table 2 along with the expected errors associated with the other sets of dynamics and data.

In the derivation of the momentum equations (Eqs. (2) and (3)), many assumptions are made and several terms are neglected. Depending on the location and time of year the largest of these tentative sources of error might differ significantly. This makes finding and estimating the primary source of error an extremely difficult task to perform. Momentum equation error estimates should be based on the magnitudes of the terms neglected. However, there is not a procedure for estimating many of the neglected terms, thus requiring estimates based on the magnitudes of known terms and the assumption that the unknown terms are comparable. Prior observations indicate that the flow through the straight is

Table 2
Estimated expected errors for the dynamics and measurements that are used to construct the weighing matrix

| | $n$ | Expected error $\langle er \rangle$ |
|---|---|---|
| Continuity | 1545 | $2.22 \times 10^{-8}$ m/s |
| Momentum | 1545 | $5.50 \times 10^{-5}$ m$^2$/s$^2$ |
| $U$ & $V$ smoothing | 1545 | $1.65 \times 10^{-7}$ l/s |
| SSH smoothing | 1545 | $7.80 \times 10^{-10}$ l/m |
| Boundary constraints | 182 | $4.87 \times 10^{-4}$ m$^2$/s |
| ADCP measurements | 12 | 2.09 m$^2$/s |
| TOPEX SSH differences | 976 | 2.18 m |

$n$ is the number of discretized equations of each dynamical and data component for each season within the coefficient matrix. These values are required in Eq. (15) so that each weighted component has an equal contribution within the total cost function (Eq. (12)). Note that the large range in values of expected error is due to the different equations and measurements having different physical representation and thus different units.

generally in geostrophic balance (Katoh, 1993). Basing error estimates on either the Coriolis force or pressure gradient therefore would be inappropriate. The combined magnitude of neglected terms is therefore approximated to be the magnitude of the wind stress. Since wind stress varies considerably throughout the year, the average of all three seasons is used to construct this expected error estimate.

The primary source of error in the boundary constraint is expected to be from neglecting the influence of river water outflow. The value for this error is estimated by considering the average river runoff of South Korea per unit length of its coastline. The average annual rainfall and landmass area of South Korea is 1.12 m/yr and 98,480 km$^2$, respectively. If the percentage of rainfall that becomes river runoff is estimated to be 33.6%, then the total average river runoff of South Korea is $V_R = 1174\,\mathrm{m}^3/\mathrm{s}$.

The primary purpose of the smoothing constraint is to filter out sub-grid scale features. Therefore, the expected error of smoothing is set equal to the reciprocal of the square of the discretization ($1/\Delta x^2$). Since smoothing is applied to both transport and SSH, the expected errors are multiplied by corresponding average magnitude values to normalize them. The average horizontal transport and SSH magnitude values are obtained from the ADCP and TOPEX data, respectively.

The primary source of measurement error is a result of using individual measurements to represent seasonally averaged transports. The expected ADCP measurement error is estimated by computing the $\mathrm{RMS}(U - \overline{U}^S) = 8.980\,\mathrm{m}^2/\mathrm{s}$, where $U$ consists of the individual transports and $\overline{U}^S$ is the seasonal-average of $U$. Similarly, the representation error caused by seasonally averaging the TOPEX data is $\mathrm{RMS}(\eta - \bar{\eta}^S) = 9.35\,\mathrm{cm}$. Because the measurements are seasonally averaged prior to assimilation, these RMS errors are divided by the equivalent degrees of freedom, $\sqrt{T/\tau}$, where $T$ is the time period spanning the seasonally averaged data and $\tau$ is the time scale of events ($\tau = 5$ days; Teague et al., 2002).

There are uncertainties in these expected error estimates. To ensure the solution is not overly sensitive to the weights in the cost function and thus to ensure that the conclusions reached within this study are well substantiated, each weight was individually varied by plus and minus one order of magnitude to simulate a wide range of terms neglected in the estimation of the expected errors. Comparison of these solutions with the solution presented in Section 5.1 reveal only subtle differences, and these differences do not change any of the discussions or conclusions reached in this study.

## 5. Results

### 5.1. General circulation

Solutions are obtained for summer, autumn, and winter of 1999–2000 by assimilating the weighted seasonally averaged ADCP and TOPEX data with the weighted barotropic dynamics (Fig. 3). The color shading represents the SSH solution, the black arrows indicate the transport solution, and the thick red arrows indicate the ADCP measurements. The ADCP measurements are included in the plots as a reference. It is important to note that the SSH solutions are biased since no SSH measurements are assimilated. The only SSH information that is included in the assimilation is

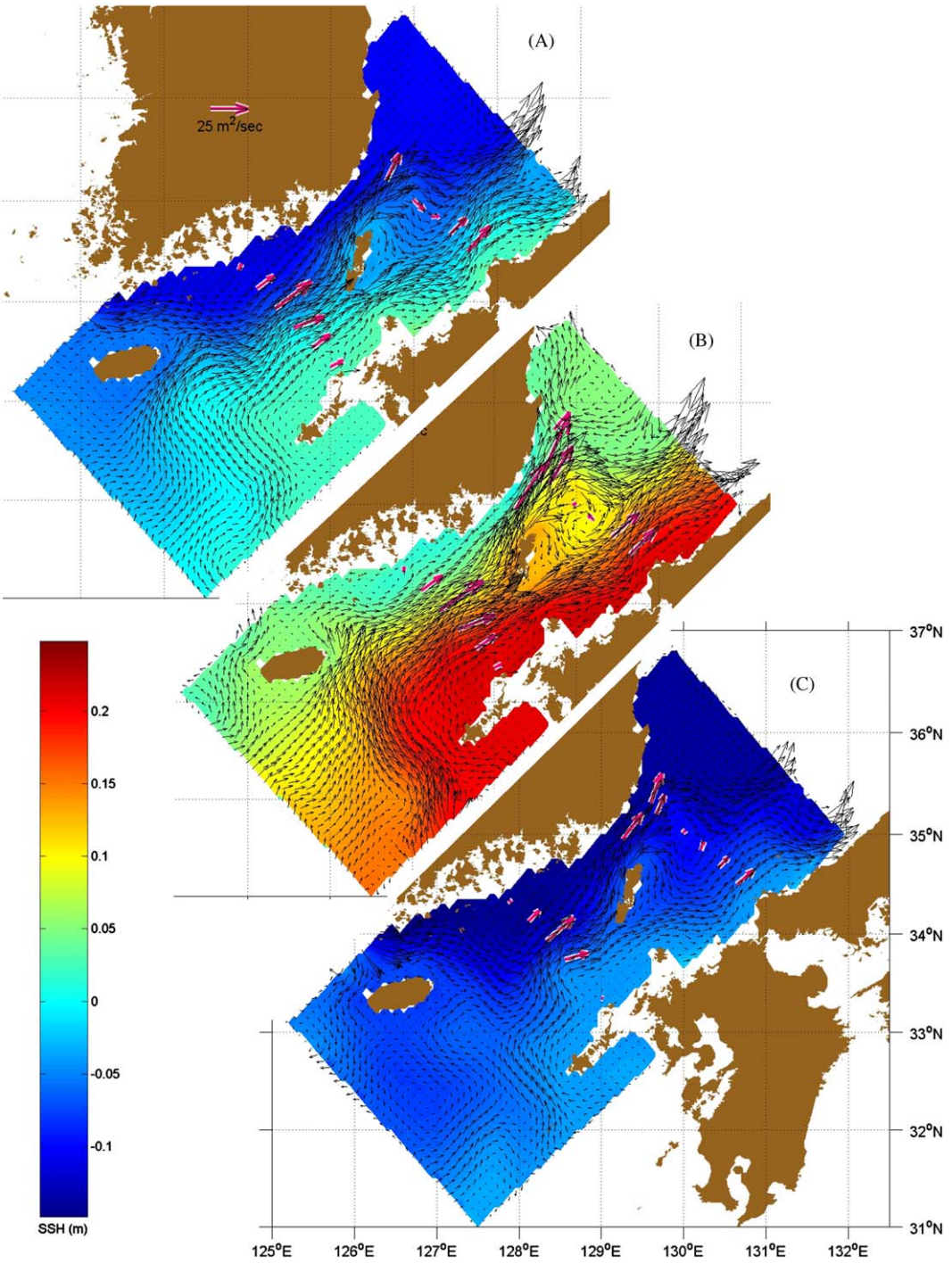


Fig. 3. The inverse solutions for the seasonal circulation for (A) summer, (B) autumn, and (C) winter are obtained by assimilating the weighted current meter and TOPEX data (shown in Fig. 2) with weighted barotropic dynamics. The black vectors represent seasonally averaged and vertically integrated velocities and the colored contours represent SSH (m). ADCP data (red vectors) are overlaid onto the figure for comparison.

the spatial and seasonal gradients of SSH inferred from the pressure gradient term and TOPEX data, respectively.

In all three seasons, the solution shows inflow through the open boundaries of the domain southwest of the strait with some flow entering through the Cheju Strait. The incoming water converges to the center of the strait just south of Tsushima Island. The flow then branches through the channels east and west of Tsushima Island, and upon exiting the strait, forms the EKWC, the NSB, and the OSB. There are significant differences in the branching of the strait outflow between the three seasonal solutions. The summer and autumn transports through the eastern channel are similar, whereas the transport through the western channel increases substantially from summer to autumn. During winter, the transport through both channels decreases considerably. In the autumn solution, there is a small cyclonic eddy just northeast of Tsushima Island. In the winter solution, there is a small anticyclonic eddy southwest of the eastern channel. This eddy is a result of there being no data at station S5 and the velocity at station S6 being directed in the southwestward direction.

The NSB and OSB are very distinct in the solutions for all three seasons. At the exit of the western channel (about 35.5° latitude), a majority of the transport branches toward the southeast following the southern ridge of the Ullung basin and contributes to the transport within the OSB. This diversion of water to the OSB causes the EKWC to be much weaker than has been observed. The dynamical equation residuals resulting from these solutions provide ancillary information needed in order to understand this result, which is discussed in Section 6.

### 5.2. Convergence of solution

In order to determine the level of dependence the solution has on just the ADCP measurements and how well these measurements constrain the system, the assimilation of TOPEX data is removed and the ADCP measurements from the two lines of moorings are separately removed. Comparison of autumn solutions using only the northern and then only the southern lines of moorings (Figs. 4B and C, respectively) with the autumn solution that uses all moorings (Fig. 4A) reveals that even with fewer measurements the solution remains fairly consistent. The spatially averaged percent difference between transport solutions that use just the northern line of moorings and all moorings is roughly 20%. Likewise, the difference using just the southern line of moorings is roughly 30%. Therefore, the solution using just the northern line of measurements is able to reproduce the full solution more accurately than using just the southern line. The reason for this result is that there is a large discrepancy between the dynamics and measurements at the exit of the western channel, which is in the northern half of the domain. The cause for this discrepancy will be analyzed in Section 5.3.

Comparison of the autumn solutions with and without the assimilation of TOPEX data (Figs. 3B and 4A, respectively) reveal that the basic structure of the flow fields is roughly the same. There is, however, a significant change in the flow field around Cheju Island. The addition of TOPEX data causes a large reduction in the CWC and a large increase in northward flow west of Cheju Island. Also, this comparison shows a significant difference in the magnitudes of SSH. This is to be expected since the SSH solution without the assimilation of TOPEX data is only a function of the pressure gradient term. By including measurements of seasonal SSH difference in the assimilation, the SSH is shifted in order for all seasonal solutions to satisfy these data. The inclusion of TOPEX data also provides additional spatial coverage that helps constrain the solution away from the ADCP mooring locations. Transport solutions away from the ADCP measurements have a higher magnitude and smaller spatial scales, which correspond to steeper SSH gradients.

Even though the TOPEX data provide useful information to the assimilation system, it is not the primary reason they were included. The main reason for this inclusion is that they help constrain the weighted least squares problem and they improve the condition number of the normal matrix. To demonstrate that adding TOPEX data improves the condition number, the values of the

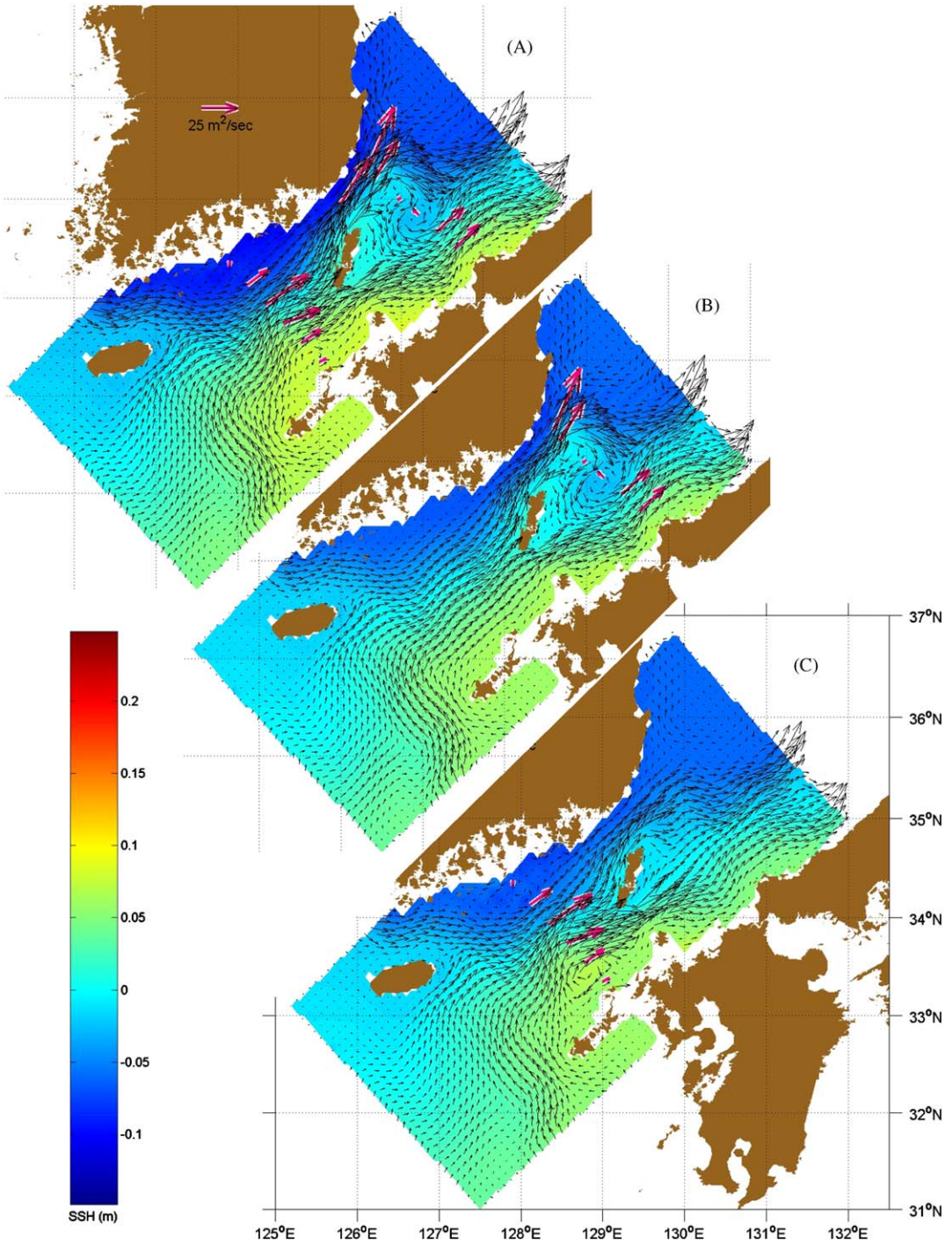


Fig. 4. Inverse solutions for autumn obtained by assimilating just the weighted current meter data (same as Fig. 3b but without the assimilation of TOPEX data). Comparison of inverse solutions resulting from the assimilation of (A) all, (B) the northern line, and (C) the southern line of current meters shows that observations match the barotropic dynamics reasonably well at the locations of the missing current meters.

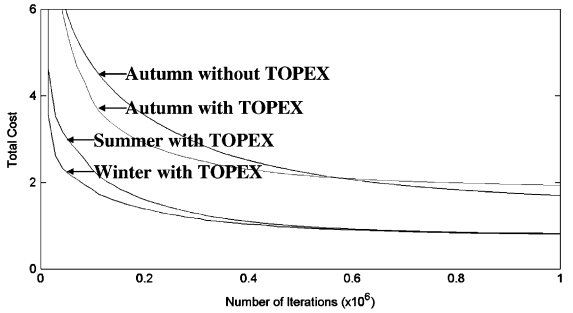


Fig. 5. The minimization of the seasonal components of the total cost function (including the assimilation of TOPEX data) as it iterates through the conjugate gradient. The displayed autumn solution without the assimilation of TOPEX data shows that reducing the number of observations increases the number of iterations required for the cost function to converge.

cost function (Eq. (12)) after each iteration of the conjugate gradient are displayed for each season (Fig. 5). The convergence of the cost function for the autumn solution without the assimilation of TOPEX data is also displayed for comparison. These curves provide a measure of how well the state satisfies all of the contributors to the total cost function, which include errors to the dynamics, constraints, and measurements. As discussed in Section 4.3, the weights for each contributor are divided by its number of equations (the number of grid points, boundary points, or measurements) such that each contributor is considered equally during the convergence of the cost function. This means that if each discretized equation from all of the contributors is exactly satisfied within expected error, then the total cost would be equal to the number of contributors (nine). The cost functions in Fig. 5 indicate that the converged solution for each season satisfies the overall contribution from dynamics, constraints, and measurements to within expected error. The total residual for the summer and winter solutions is within 10% of the expected error. This plot also shows that the solution for winter satisfies the overall specified barotropic dynamics the best, and the autumn solution contains the largest discrepancies between the dynamics and data.

However, even though the solutions are converged, the number of iterations that are required to achieve this convergence is more than optimal. As mentioned in Section 4.2, one to three loops through the conjugate gradient routine is typically sufficient to obtain a converged solution for a well-conditioned system, where each loop consists of the number of iterations equal to the size of the state. The autumn solution without the assimilation of TOPEX data requires 250 loops (roughly 1.1 million iterations) through the conjugate gradient to converge (Fig. 5). Even after this many iterations, the total cost still has a slight downward trend, indicating the problem is poorly conditioned without the assimilation of TOPEX data. Whereas, the autumn solution with the assimilation of TOPEX data only requires 75 loops (roughly 1 million iterations) through the conjugate gradient in order to converge. Note that the inclusion of TOPEX data requires all three seasonal solutions to be solved simultaneously. Therefore, the size of the state and hence the number of iterations contained in one loop is three times larger than that without the assimilation of TOPEX data. In other words, the total number of iterations required to solve all three seasonal solutions with the assimilation of TOPEX data is less than that required to solve one season without TOPEX data.

### 5.3. Dynamic residuals

Since the computed solutions are a best fit to the equations of motion, constraints, and measure-

Table 3
Spatially averaged residuals of each component of the barotropic dynamics and data for each season divided by corresponding expected errors

| | Summer | Autumn | Winter |
|---|---|---|---|
| Continuity | 5.317e-4 | 8.761e-4 | 5.456e-4 |
| Momentum | 0.5256 | 0.9107 | 0.5791 |
| $U$ & $V$ smoothing | 0.2174 | 0.3076 | 0.2074 |
| SSH smoothing | 0.0526 | 0.0771 | 0.0517 |
| Boundary constraints | 1.620e-4 | 2.321e-4 | 1.508e-4 |
| ADCP measurements | 0.0420 | 0.0539 | 0.0403 |
| TOPEX SSH differences | 0.6650 | | 0.9525 |

The units of these residuals are in number of standard deviations (Std) of the corresponding expected errors.

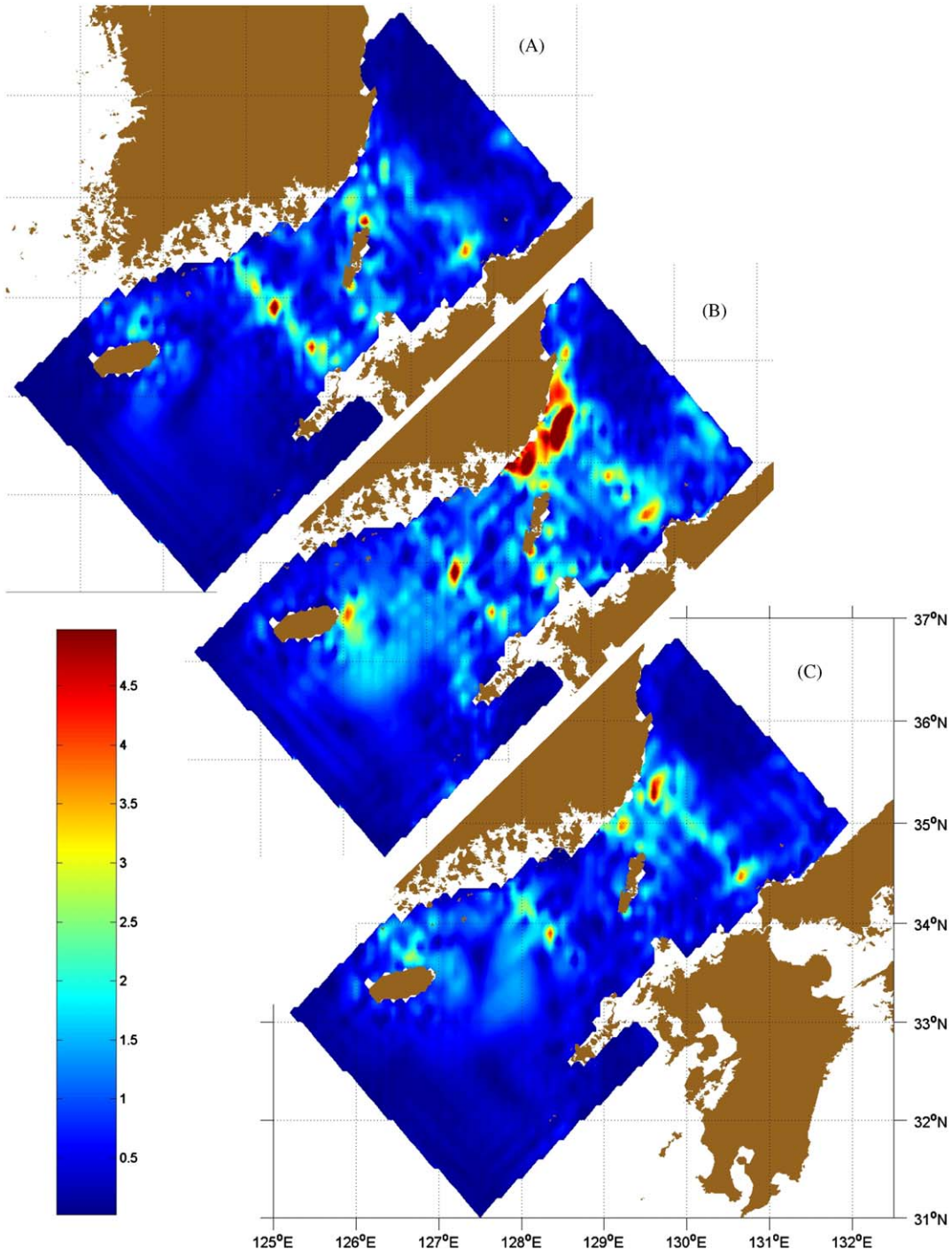


Fig. 6. The momentum equation residuals show where during the (A) summer, (B) autumn, and (C) winter seasons that the assumed barotropic dynamics are in error. These residuals are in units of number of standard deviations (Std) relative to the expected error and are considered significant if they are greater than 3 Std. The largest residuals occur in autumn at the exit of the western channel. It is in this area that baroclinic dynamics are expected to be important based on previous studies.

ments, the solution is going to satisfy none of these exactly (Eq. (11)). The dynamic and measurement residuals are computed and examined in order to determine how well the solutions satisfy the assumed barotropic dynamics. The absolute value of these residuals is divided by the corresponding expected errors ($|\mathbf{Ax}-\mathbf{b}|/\langle er\rangle$) to identify areas in which residuals are much larger than expectations. These resulting measures of error are therefore in terms of number of standard deviations (Std) of the expected error. Spatial averages of the normalized residuals are displayed in Table 3 for each component and season, and give an overall indication of how well the solution satisfies the prescribed dynamics and measurements. In general, the spatially averaged normalized residuals are roughly equivalent for summer and winter, whereas for autumn these residuals are higher. The mean residuals show that continuity and the boundary constraints are satisfied well within expected values, residuals in the smoothing of SSH and the ADCP data are within 0.1 Std, residuals in the smoothing of horizontal transport are within 0.5 Std, and agreement to the momentum equations and the TOPEX measurements are within 1 Std. The distribution of the normalized barotropic momentum equation residuals (Fig. 6) indicates that the solution satisfies the assumed dynamics to within 1 Std of expected values over most of the domain, especially during winter. There are, however, small pockets of relatively large error at some of the ADCP mooring locations during all three seasons, and a large area of error at the exit of the western channel during autumn. At these locations, momentum equation residuals exceed 3 Std of the expected error.

It is believed that the significantly large momentum residual at the exit of the western channel during autumn is a result of the barotropic momentum equations not being able to resolve baroclinic processes. Observations have been made in previous studies that suggest that strong baroclinic processes occur in this region and peak during this season (Isobe, 1995). To test this theory, solutions are computed by assimilating the ADCP and TOPEX measurements with the 2.5-layered baroclinic system of equations discussed in Section 3.2. The spatially averaged residuals relative to their expected values resulting form this assimilation are presented in Table 4 for each component, season, and layer. Comparison of these residuals with those resulting from using the barotropic system of equations (Table 3) reveals that the mean residuals of continuity, smoothing, and the boundary constraint have comparable values. The mean residuals of the momentum equations, ADCP data, and TOPEX data, however, are roughly half in the 2.5-layered baroclinic system compared to the corresponding residuals in the barotropic system. Thus, the baroclinic momentum equations are in better agreement with the measurements than the barotropic momentum equations. By comparing the distribution of momentum residuals during autumn between these two systems of equations (Fig. 7), it is apparent that the inclusion of baroclinic processes in the momentum equations reduces the residual at the exit of the western channel.

Table 4
Spatially averaged residuals of each component of the baroclinic dynamics and data for each season and layer divided by corresponding expected errors

| | | Summer | Autumn | Winter |
|---|---|---|---|---|
| Continuity | Layer 1 | 5.856e-4 | 4.130e-4 | 4.121e-4 |
| | Layer 2 | 0.0972 | 0.1373 | 0.0916 |
| Momentum | Layer 1 | 0.3538 | 0.5346 | 0.3968 |
| | Layer 2 | 0.4620 | 0.5665 | 0.3939 |
| $U$ & $V$ smoothing | Layer 1 | 0.2096 | 0.2847 | 0.1805 |
| | Layer 2 | 0.3304 | 0.4175 | 0.2389 |
| $\eta$ smoothing | Layer 1 | 0.0674 | 0.0860 | 0.0532 |
| | Layer 2 | 0.2769 | 0.3559 | 0.2221 |
| | Layer 3 | 0.0504 | 0.0542 | 0.0362 |
| Boundary constraints | Layer 1 | 1.240e-4 | 1.591e-4 | 1.360e-4 |
| | Layer 2 | 1.577e-4 | 1.969e-4 | 1.752e-4 |
| ADCP measurements | Layer 1 | 0.0220 | 0.0486 | 0.0276 |
| | Layer 2 | 0.0307 | 0.0283 | 0.0182 |
| TOPEX SSH differences | | 0.3702 | | 0.5002 |

The units of these errors are in number of standard deviations (Std) of the corresponding expected errors.

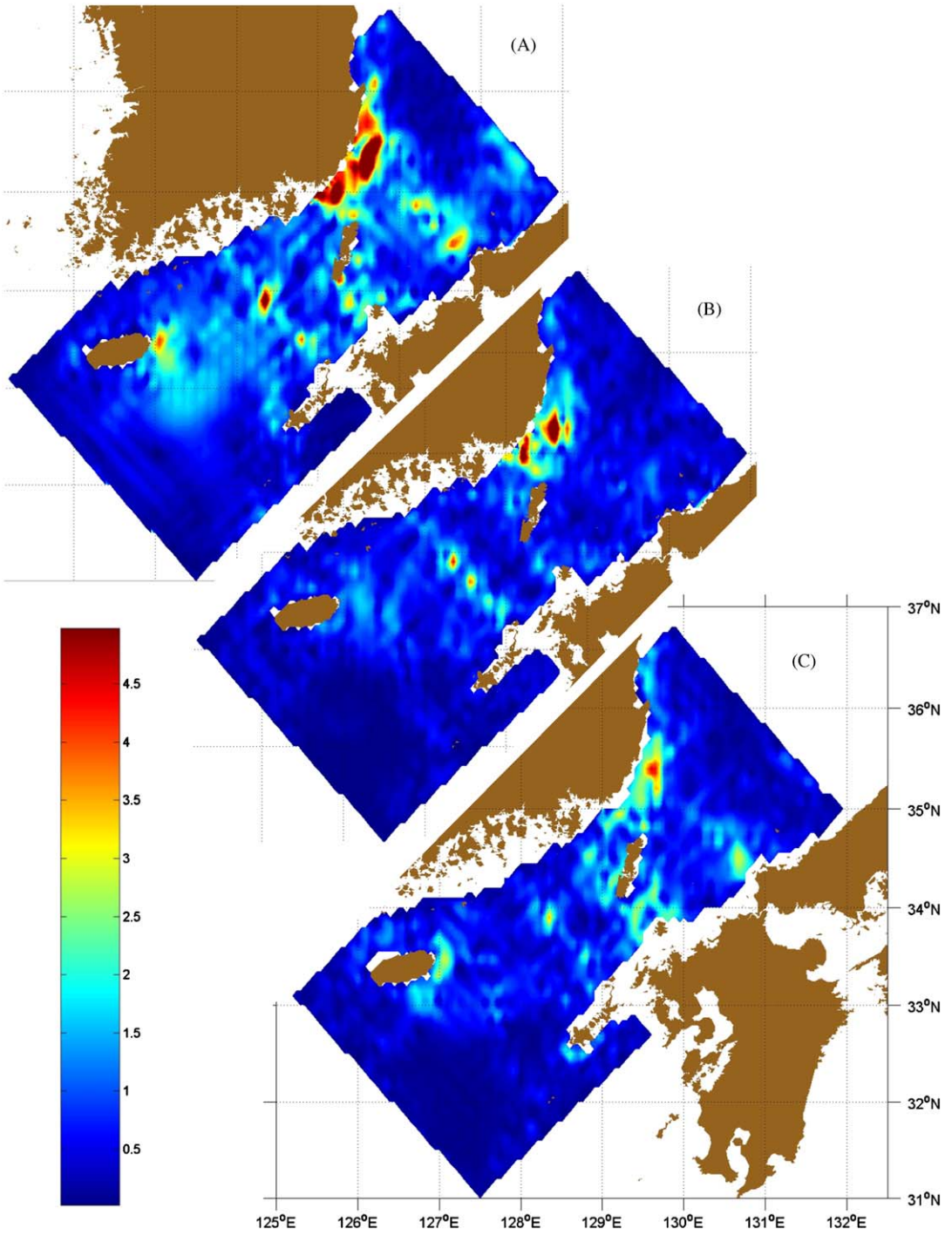


Fig. 7. The residuals of the (A) barotropic momentum equations and the (B) surface and (C) second-layer baroclinic momentum equations for autumn show that the inclusion of baroclinic effects in the dynamics reduces momentum equation residual, especially at the exit of the western channel.

## 6. Discussion and conclusions

Velocity and SSH measurements are assimilated with both a system of single-layered barotropic and 2.5-layered baroclinic equations for the summer, autumn, and winter seasons of 1999–2000 using a variational assimilation approach. Since the weighted data and dynamics cannot be expected to match each other exactly, the optimal solution will cause residuals in both. The barotropic momentum equation residuals (Fig. 6) reveal that the best-fit solution does not satisfy the assumed dynamics within expected values at the exit of the western channel during autumn. The location and season of this large momentum residual coincide with the region and time of year that have been observed in previous studies to exhibit baroclinic dynamics. For example, Isobe (1995) assimilates ADCP-CTD survey data into a 5-layered model for the summer and a 2-layered model for the winter, and demonstrates that the observed seasonal variability in the sea-level difference across the Tsushima/Korean Strait just north of Tsushima Island largely contains the baroclinic motion caused by the Bottom Cold Water (BCW), which is believed to originate in the Japan/East Sea and penetrate almost exclusively into the western channel. Isobe (1995) also concludes that the sea level differences across the strait is 8 cm in the summer and 3 cm in the winter, which corresponds with the amount of BCW observed in the western channel being at its maximum during summer and minimum during winter.

In a more recent hydrographic study, Cho and Kim (2000) observed the BCW moving up onto the shelf of the western channel during summer and retreating back to the Ullung basin during winter. In addition to showing the nonexistence of the BCW during winter, observations were made that indicate that the EKWC is also absent during this season. Cho and Kim (2000) explain that when the lower layer is absent, the northward flow in the upper layer has a positive relative vorticity due to the increasing depth from south to north, therefore causing the flow exiting the western channel to veer eastward. In contrast during summer, the existence of the BCW causes the upper layer to shrink as the flow moves northward, therefore creating negative relative vorticity and causing the EKWC to flow along the western boundary.

In the barotropic results (Fig. 3), the EKWC is virtually nonexistent during summer and winter and weaker than observed during autumn. Since the barotropic dynamics do not account for the baroclinic effects of the BCW, then according to Cho and Kim's (2000) hypothesis it is consistent that the flow exiting the western channel in these results veers eastward instead of forming the EKWC. The assimilation of measurements with a 2.5-layered baroclinic system of equations shows that the incorporation of baroclinic effects results in a significant reduction in momentum error at the exit of the western channel during autumn (Fig. 7). This implies that there is a failure of the barotropic approximation within this region. Even though it is widely believed that the flow through the Tsushima Strait is mostly barotropic, the results from this study indicate that some other processes are prevalent at the exit of the western channel and are capable of seriously affecting the overall dynamics of the flow. The most plausible source of these processes within this area is baroclinic forcing.

## Acknowledgements

This work was sponsored by the Office of Naval Research (program element PE0601153N) as part of the projects "Dynamical Linkage of the Asian Marginal Seas" and "Error Propagation in the Continental Shelf". This work is a contribution of the Naval Research Laboratory, No. JA/7323-98-0068.

## References

Cho, Y., Kim, K., 1998. Structure of the Korea Strait Bottom Cold Water and its seasonal variation in 1991. Continental Shelf Research 18, 791–804.

Cho, Y., Kim, K., 2000. Branching mechanism of the Tsushima Current in the Korea Strait. Journal of Physical Oceanography 30, 2788–2797.

Csanady, G., 1984. Circulation in the Coastal Ocean. Reidel Publishing Co., Dordrecht, Holland.

Daley, R., 1993. Atmospheric Data Analysis. Cambridge University Press, Cambridge, NY.

Fox, D.N., Teague, W.J., Barron, C.N., 2002. The Modular Ocean Data Assimilation System (MODAS). Journal of Atmospheric and Oceanic Technology 19, 240–252.

Fu, L., Christensen, E.J., Yamarone, C.A., Lefebvre, M., Menard, Y., Dorrere, M., Esculdier, P., 1994. TOPEX/POSEIDON mission overview. Journal of Geophysical Research 99, 24,369–24,381.

Isobe, A., 1995. The influence of the Bottom Cold Water on the seasonal variability of the Tsushima Warm Current. Continental Shelf Research 15, 763–777.

Isobe, A., Tawara, S., Kaneko, A., Kawano, M., 1994. Seasonal variability in the Tsushima Warm Current, Tsushima-Korea Strait. Continental Shelf Research 14, 23–35.

Jacobs, G.A., Perkins, H.T., Teague, W.J., Hogan, P.J., 2001a. Summer transport through the Tsushima-Korea Strait. Journal of Geophysical Research 106, 6917–6930.

Jacobs, G.A., Book, J.W., Perkins, H.T., Teague, W.J., 2001b. Inertial oscillations in the Korea Strait. Journal of Geophysical Research 106, 26943–26957.

Jacobs, G.A., Whitmer, K.R., Barron, C.N., Klingenberger, S., May, D.N., Blaha, J.P., 2002. Operational altimeter sea level products. Oceanography 15, 13–21.

Katoh, O., 1993. Detailed current structures in the eastern channel of the Tsushima Strait in summer. Journal of Oceanography 49, 17–30.

Kim, K., Legeckis, R., 1986. Branching of the Tsushima Current in 1981–83. Progress in Oceanography 17, 265–276.

Le Dimet, F.X., Talagrand, O., 1986. Variational algorithms for analysis and assimilation of meteorological observations: theoretical aspects. Tellus 38A, 97–110.

Miita, T., Ogawa, Y., 1984. Tsushima currents measured with current meters and drifters. In: Ichiye, T. (Ed.), Ocean Hydrodynamics of the Japan and East China Seas. Elsevier Science Publishing Co., New York, pp. 67–76.

Perkins, H.T., Teague, W.J., Jacobs, G.A., 2000. Currents in Korea-Tsushima Strait during summer 1999. Geophysical Research Letters 27, 3033–3036.

Pond, S., Pickard, G., 1983. Introductory Dynamical Oceanography, second ed. Butterworth-Heinemann, Oxford, England.

Teague, W.J., Perkins, H.T., Jacobs, G.A., Book, J.W., 2001. Tide observations in the Korea-Tsushima Strait. Continental Shelf Research 21, 545–561.

Teague, W.J., Jacobs, G.A., Perkins, H.T., Book, J.W., Chang, K.I., Suk, M.S., 2002. Low frequency current observations in the Korea/Tsushima Strait. Journal of Physical Oceanography 32, 1621–1641.

Thacker, W.C., 1992. Oceanographic inverse problems. Physica D 60, 16–37.

Wunsch, C., 1996. The Ocean Circulation Inverse Problem. Cambridge University Press, New York.